Acta Geotechnica (2018) 13:367–386
https://doi.org/10.1007/s11440-017-0548-y

RESEARCH PAPER

An ISA-plasticity-based model for viscous and non-viscous clays

W. Fuentes[1] · **M. Tafili**[2] · **Th. Triantafyllidis**[2]

Received: 18 July 2016 / Accepted: 23 March 2017 / Published online: 22 April 2017
© Springer-Verlag Berlin Heidelberg 2017

Abstract The ISA-plasticity is a mathematical platform which allows to propose constitutive models for soils under a wide range of strain amplitudes. This formulation is based on a state variable, called the intergranular strain, which is related to the strain recent history. The location of the intergranular strain can be related to the strain amplitude, information which is used to improve the model for the simulation of cyclic loading. The present work proposes an ISA-plasticity-based model for the simulation of saturated clays and features the incorporation of a viscous strain rate to enable the simulation of the strain rate dependency. The work explains some aspects of the ISA-plasticity and adapts its formulation for clays. At the beginning, the formulation of the model is explained. Subsequently, some comments about its numerical implementation and parameters determination are given. Finally, some simulations are performed to evaluate the model performance with two different clays, namely a Kaolin clay and the Lower Rhine clay. The simulations include monotonic and cyclic tests under oedometric and triaxial conditions. Some of these experiments include the variation of the strain rate to evaluate the viscous component of the proposed model.

Keywords Clays · Constitutive models · Cyclic loading · ISA-plasticity · Viscosity

✉ W. Fuentes
fuentesw@uninorte.edu.co

[1] University del Norte, Km.5 Va Puerto Colombia, Barranquilla, Colombia

[2] Institute of Soil Mechanics and Rock Mechanics, Karlsruhe Institute of Technology KIT, Engler-Bunte-Ring 14, 76131 Karlsruhe, Germany

1 Introduction

Simulations of geotechnical structures dealing with saturated clays require in many cases a realistic description of the soil under monotonic and cyclic loading, e.g., [5, 9, 10, 28, 54]. The behavior of this material depends not only on the material state, such as the effective stress or density, but also on the strain amplitude [3, 4]. Researchers have found that the clay behaves elastically only under very small strain amplitudes, of about $\| \Delta\boldsymbol{\varepsilon} \| < 10^{-4}$. Under medium strain amplitudes, the so-called small strain effects $10^{-4} < \| \Delta\boldsymbol{\varepsilon} \| < 10^{-2}$ take place, namely the stiffness increase due to reversal loading and the reduction of the plastic strain rate [19, 37]. The stiffness amplifying factor reduces for increasing strain amplitudes, as observed on a typical stiffness degradation curve. Finally, when the soil is sheared under very large deformations $\| \Delta\boldsymbol{\varepsilon} \| > 10^{-2}$, it tends asymptotically to the critical state responsible for the failure. These are at least some relevant aspects which are expected to be considered by competent constitutive models.

A single model capturing all these effects is rare to find, and therefore, researchers recommend the usage of an "appropriated" model for each particular problem. To give an example, one would choose some elastoplastic models [11, 42, 45, 56], a Karlsruhe hypoplastic model for clays [24, 26, 35, 55] or a Barodesy model for clays [15, 36] for the simulation of a bearing capacity problem of a shallow foundation. These models are only able to simulate monotonic loading for non-viscous clays, and therefore, they would not capture the strain rate dependency typical for plastic clays. If the clay shows a high plasticity, a rate-dependent model could be useful to consider the influence of the loading velocity, e.g., [7, 8, 30, 40, 44, 62, 63]. All

the mentioned models limit their capabilities for monotonic loading, and therefore, their use is very restricted. In contrast, in problems where the soil exhibits unloaded zones, such as urban excavations with retaining walls, small strain effects should be certainly considered [12] and robust models to simulate memory effects, e.g., [25], or cyclic loading are probably required, e.g., [14, 32, 33, 46, 49, 51]. Finally, if the problem deals only with small strain amplitudes $\| \Delta\boldsymbol{\varepsilon} \| < 10^{-4}$, as for example a wave propagation problem, an elastic relation describing the stiffness for small strains and depending on the material state would be sufficient for the material model [23, 47]. Hence, as one may see, the type of constitutive model varies substantially depending on the problem type and sometimes one may loose the connection between their mathematical formulations.

Among all the types of constitutive models, an interesting approach called ISA-plasticity has been recently proposed by Fuentes and Triantafyllidis [19] intending to embrace a wide range of strain amplitudes with a single constitutive equation. The ISA-plasticity (Intergranular Strain Anisotropy) presents a general mathematical formulation which adapts its equation to the proper one depending on the strain amplitude. In particular, the model recognizes a small strain amplitude at which only elastic behavior occurs, a medium strain amplitude whereby small strain effects are considered, and a large strain amplitude where all these small strain effects cease. It allows also to extent the capabilities of existing hypoplastic models [24, 29, 35, 55, 59, 60] for the simulation of cyclic loading and small strain effects. The first ISA-plasticity-based model was proposed for sands [16, 19] and proved to simulate fairly well the behavior in a wide range of strain amplitudes. Recently, this formulation was coupled with the hypoplastic model of Wolffersdorff [59] to simulate a larger number of consecutive cycles ($N > 30$) and complex multidimensional loading [43]. So far, an ISA-plasticity-based model for viscous clays has never been proposed in the literature, although some hints were given in [17] to simulate non-viscous clays.

In this work, an ISA-plasticity-based formulation is proposed to simulate the monotonic and cyclic behavior of saturated clays. An extension is also proposed to simulate the strain rate dependency shown by some clays. In contrast to most of the conventional models, the strain rate dependency is simulated by an additional strain mechanism whose intensity depends on the material viscosity. The extension proposed by Poblete et al. [43] to enhance the ISA-plasticity for a larger number of repetitive loading ($N > 30$) is accounted in the present work. The structure of this article is as follows: At the beginning, the formulation of the proposed model is explained. Then, a short guide to determine its parameters is provided. Finally some simulations are carefully analyzed to discuss the model performance. The notation of this article is as follows. Scalar quantities are denoted with italic fonts (e.g., a,b), second-rank tensors with bold fonts (e.g., $\mathbf{A}, \boldsymbol{\sigma}$) and fourth-rank tensors with Sans Serif type (e.g., E, L). Multiplication with two dummy indices, also known as double contraction, is denoted with a colon " : " (e.g., $\mathbf{A} : \mathbf{B} = A_{ij}B_{ij}$). When the symbol is omitted, it is then interpreted as a dyadic product (e.g., $\mathbf{AB} = A_{ij}B_{kl}$). The deviatoric component of a tensor is symbolized with an asterisk as superscript $\mathbf{A}^*$. The effective stress tensor is denoted with $\boldsymbol{\sigma}$ and the strain tensor with $\boldsymbol{\varepsilon}$. The Roscoe invariants are defined as $p = -\mathrm{tr}\boldsymbol{\sigma}/3$, $q = \sqrt{3/2} \| \boldsymbol{\sigma}^* \|$, $\varepsilon_v = -\mathrm{tr}\boldsymbol{\varepsilon}$ and $\varepsilon_s = \sqrt{2/3} \| \boldsymbol{\varepsilon}^* \|$. The stress ratio tensor is defined as $\mathbf{r} = \boldsymbol{\sigma}^*/p$.

2 ISA-plasticity formulation with viscous strain

The ISA-plasticity is a family of constitutive models able to describe the monotonic and cyclic behavior of soils. Its key characteristics among other models are to incorporate the strain amplitude dependency and to simulate small strain effects. Accordingly, the elastic locus of the material is enclosed by the size of a strain amplitude denoted with $\| \Delta\boldsymbol{\varepsilon} \| = R$, commonly known as the threshold strain [1, 52]. This strain amplitude takes a value of approximately $R \approx 10^{-4}$ for clays according to some experiments reporting shear modulus degradation curves [1, 52]. The ISA-plasticity can be cataloged as an elastoplastic model, but in contrast to conventional models, its yield surface is defined within the space of a state variable related to the strain amplitude. This variable is a second-rank tensor called the intergranular strain and denoted with $\mathbf{h}$. It was originally introduced by Niemunis and Herle [39] to improve some existing hypoplastic models (e.g., [59]) but entirely reformulated by Fuentes and Triantafyllidis [19] to incorporate the elastic locus of the material. Although both formulations present similar parameter meanings, they operate in different ways and do not share any mathematical relation. The general formulation of the ISA-plasticity has been tackled in former works [16, 19, 43]; however, some aspects are in the following sections explained. In Sect. 2.1, the evolution equation of the intergranular strain $\mathbf{h}$ will be described. Subsequently, the mechanical model formulation relating the stress rate $\dot{\boldsymbol{\sigma}}$ to the strain rate $\dot{\boldsymbol{\varepsilon}}$ is explained (Sect. 2.2). The general formulation of the mechanical model features for this work the incorporation of a viscous strain rate to simulate the strain rate dependency of the material. This and other details of the mechanical model will be explained in Sect. 2.2.

2.1 Evolution equation of the intergranular strain

In this section the evolution of the intergranular strain $\mathbf{h}$ is described. Detailed description of these relations can be also found in [16, 19, 22, 43] but will be summarized in the following lines. The equation for the rate $\dot{\mathbf{h}}$ is based on a simple elastoplastic relation which reads:

$$\dot{\mathbf{h}} = \dot{\boldsymbol{\varepsilon}} - \dot{\lambda}_H \mathbf{N} \tag{1}$$

whereby $\dot{\boldsymbol{\varepsilon}}$ is the strain rate, $\lambda_H \geq 0$ is a consistency parameter, also known as plastic multiplier, and $\mathbf{N}$ is the flow rule ($\| \mathbf{N} \| = 1$) considered as associative, i.e., normal to the yield surface. Under elastic conditions, the consistency parameter is equal to $\lambda_H = 0$ and the intergranular strain $\mathbf{h}$ evolves identically as the strain $\boldsymbol{\varepsilon}$, i.e., $\dot{\mathbf{h}} = \dot{\boldsymbol{\varepsilon}}$. The aforementioned feature allows us to introduce a yield surface related to the strain amplitude $\| \Delta\boldsymbol{\varepsilon} \| = R$ through the following yield function F_{H}:

$$F_{\mathrm{H}} = \| \mathbf{h} - \mathbf{c} \| - R/2 \tag{2}$$

whereby $\mathbf{c}$ is a hardening variable of the intergranular strain model and describes the center of the yield surface. This variable has been also termed the back-intergranular strain [19] considering its kinematic mechanism. As in conventional elastoplasticity, an elastic condition is described through the condition $F_{\mathrm{H}} < 0$ while $F_{\mathrm{H}} = 0$ implies plasticity. The shape of the yield surface is very simple: It describes a perfect sphere within the principal space of the intergranular strain space as depicted in Fig. 1a. The yield surface turns into a circle within the space of the invariants $h_v = -tr(\mathbf{h})$ and $h_s = \sqrt{2/3}\|\mathbf{h}^*\|$, where $\mathbf{h}^*$ is the deviatoric intergranular strain; see Fig. 1b. The outer (green) surface corresponds to the bounding surface of the intergranular strain which will be explained later on. The flow rule is normalized $\| \mathbf{N} \| = 1$ and is normal to the yield surface and therefore reads:

$$\mathbf{N} = (\mathbf{h} - \mathbf{c})^{\rightarrow} \tag{3}$$

where the operator $\sqcup^{\rightarrow} = \sqcup / \| \sqcup \|$ means normalization of an arbitrary tensor $\sqcup$. The back-intergranular strain $\mathbf{c}$ bases its evolution equation on a simple relation of bounding surface plasticity [13], but within the intergranular strain space. Its general formulation may be written as:

$$\dot{\mathbf{c}} = \dot{\lambda}\bar{\mathbf{c}} \tag{4}$$

whereby $\bar{\mathbf{c}}$ is the hardening function. The hardening rule for $\mathbf{c}$ considers a bounding surface within the intergranular strain space described with the bounding condition $F_{Hb} = 0$, whereby the function F_{Hb} is defined as:

$$F_{Hb} = \| \mathbf{h} \| - R \tag{5}$$

Notice that the bounding condition is equivalent to the constraint $\| \mathbf{c} \| \leq R/2$, as depicted in Fig. 1b. Therefore, the ISA-plasticity introduces an image tensor of $\mathbf{c}$ for the bounding condition, denoted with $\mathbf{c}_b$ and mapped as follows:

$$\mathbf{c}_b = (R/2)\overrightarrow{\dot{\boldsymbol{\varepsilon}}} \qquad \text{for} \quad \mathrm{F_{Hb}} = 0 \tag{6}$$

In order to force the bounding constraint $\dot{\mathbf{c}} = \mathbf{0}$ when $\mathbf{c} = \mathbf{c}_b$, the following relation for the hardening function $\bar{\mathbf{c}}$ has been proposed:

$$\bar{\mathbf{c}} = \beta_h(\mathbf{c}_b - \mathbf{c})/R \tag{7}$$

whereby β_h is a material parameter controlling the rate of $\mathbf{c}$. Increasing values of β_h would simulate a brittle behavior between the elastic and plastic state and vice-versa. The

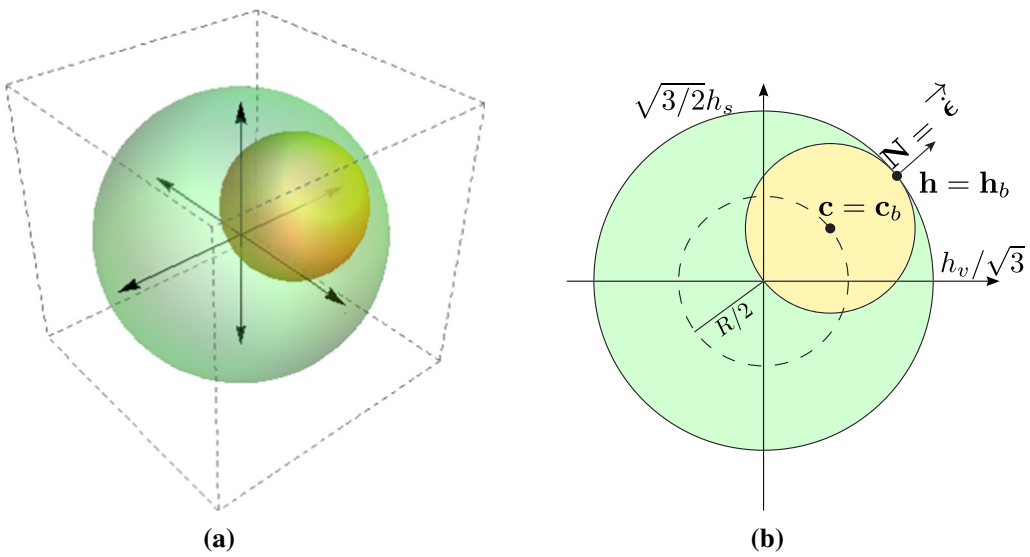

Fig. 1 Yield surface and bounding surface of the intergranular strain model. **a** 3D representation, **b** example of the bounding condition $F_{Hb} = 0$

evolution mechanism for the intergranular strain can be understood with the following example: Consider we would like to perform a monotonic loading by applying constant strain rate or a proportional strain path in the sense of Gudehus [21]. Consider also that at the beginning the intergranular strain lies at the bounding surface as shown in Fig. 2a. The strain path to apply is the one shown in Fig. 2b. At the beginning, the intergranular strain goes through the elastic locus and evolves identically to the strains, i.e., from points A to B, one obtains $\Delta\mathbf{h} = \Delta\boldsymbol{\varepsilon}$. Afterward, a plastic behavior is obtained and therefore the intergranular strain starts to decelerate according to Eq. (1). Finally, when the strain path is sufficiently large, the intergranular strain $\mathbf{h}$ reaches its image at the bounding surface $\mathbf{h} = \mathbf{h}_b$ at Point C and stops evolving $\dot{\mathbf{h}} = \mathbf{0}$; see Fig. 2a. One can show that this image tensor $\mathbf{h}_b$ reads:

$$\mathbf{h}_b = R\mathbf{N} \tag{8}$$

This particular state is called "mobilized state" and represents a state at which the soil has recently experienced medium or large deformations, of about $\| \Delta\boldsymbol{\varepsilon} \| > 10^{-3}$ or even more. At this state, no small strain effects, such as stiffness, increase due to reversal loading and reduction of the plastic strain rate should be delivered by the mechanical model which is explained in the following section.

The consistency parameter $\dot{\lambda}_H$ is derived from the consistency equation $\dot{F}_H = 0$ and reads [19] :

$$\dot{\lambda}_H = \frac{\langle \mathbf{N} : \dot{\boldsymbol{\varepsilon}} \rangle}{1 - \left(\dfrac{\partial F_H}{\partial \mathbf{c}} \right) : \bar{\mathbf{c}}} \tag{9}$$

The set of Eqs. (1)–(9) defines the intergranular strain model. The main purpose of the information provided by the intergranular strain is to improve the mechanical constitutive model for cyclic loading. According to the proposed theory, if the intergranular strain $\mathbf{h}$ is far away from its image $\mathbf{h}_b$, probably the current strain amplitude is of small or medium size ($\| \Delta\boldsymbol{\varepsilon} \| < 10^{-3}$), while a mobilized state $\mathbf{h} = \mathbf{h}_b$ is a sign of larger strain amplitudes. Hence, as one may see, the current strain amplitude may be related to the relative position of the intergranular strain to its image $\|\mathbf{h}_b - \mathbf{h}\|$. This information will be very useful to improve the mechanical model in the next section and will be acquired through a suitable scalar function ρ ranging between $0 \leq \rho \leq 1$ and defined as:

$$\rho = 1 - \frac{\|\mathbf{h}_b - \mathbf{h}\|}{2R} \tag{10}$$

A value of $\rho = 1$ implies mobilized states, while $\rho \approx 0$ suggests the consideration of small strain effects. Its interpretation is very easy and therefore will be used for the mechanical model formulation.

2.2 Formulation of mechanical model for viscous soils

In this section, the general form of the constitutive equation for the mechanical behavior is explained. In contrast to the previous works, we extend the capabilities of the mechanical model to consider the strain rate dependency shown by some saturated clays. The extension is simple because it only incorporates an additional strain rate component, denoted with $\dot{\boldsymbol{\varepsilon}}^{\text{vis}}$, to simulate the viscous effects of the material. The new constitutive equation reads:

$$\dot{\boldsymbol{\sigma}} = \mathsf{E} : (\dot{\boldsymbol{\varepsilon}} - \dot{\boldsymbol{\varepsilon}}^{p} - \dot{\boldsymbol{\varepsilon}}^{\text{vis}}) \tag{11}$$

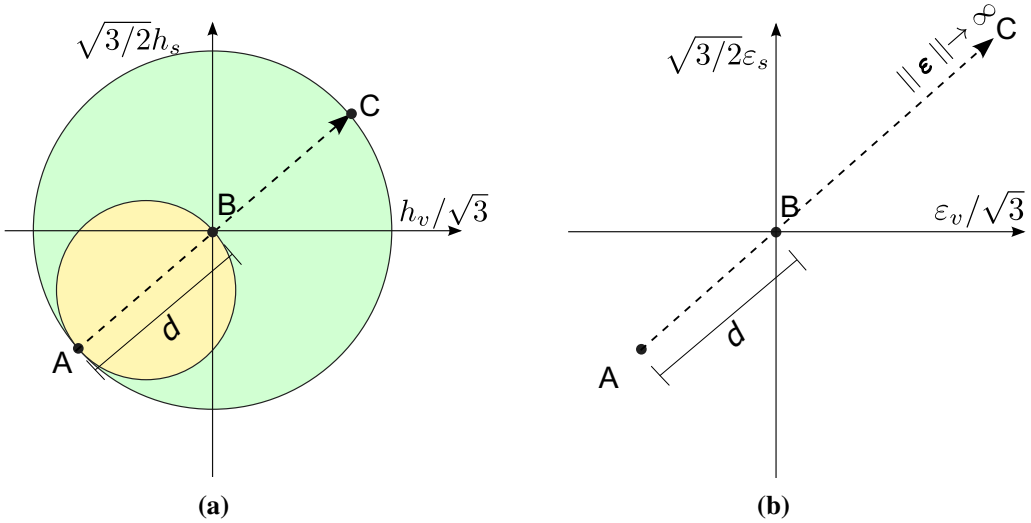

Fig. 2 Schematic illustration of the evolution of the intergranular strain. **a** Path within the intergranular strain space, **b** path within the strain space

where E is the elastic stiffness, $\dot{\boldsymbol{\varepsilon}}^{p}$ is the plastic strain rate, and $\dot{\boldsymbol{\varepsilon}}^{\text{vis}}$ is the viscous strain rate. We recall that Eq. (11) can be considered as a general case and reduces to the case of non-viscous soil when setting $\dot{\boldsymbol{\varepsilon}}^{\text{vis}} = \mathbf{0}$, as in the former works [19, 43]. The proposed formulation assumes that small strain effects do not influence the viscous strain rate $\dot{\boldsymbol{\varepsilon}}^{\text{vis}}$, and therefore is always active even under elastic conditions. We present the following two arguments to support the latter assumption: The first is to allow the simulation of creep under elastic conditions $F_{\text{H}} < 0$. In the opposite scenario, any infinitesimal unloading path (elastic step) would result in the elimination of any creep process. No experimental observation has proved such effect, and actually they show something different [40]. The second is the lack of experimental studies trying to understand the influence of the small strain effects on the strain rate dependency. We therefore opt for simplicity and let this investigation for further improvements. The magnitudes E and $\dot{\boldsymbol{\varepsilon}}^{p}$ are kept with the same structure as in [19] and read:

$$\mathsf{E} = m\bar{\mathsf{E}} \tag{12}$$

$$\dot{\boldsymbol{\varepsilon}}^{p} = y_h \dot{\bar{\boldsymbol{\varepsilon}}}^{p} \tag{13}$$

where $\bar{\mathsf{E}}$ and $\dot{\bar{\boldsymbol{\varepsilon}}}^{p}$ are called "mobilized" stiffness and "mobilized" plastic strain rate, respectively, and the factors m and y_h are scalar functions, to increase the stiffness and reduce the plastic strain rate upon reversal loading, respectively. Their formulation reads:

$$y_h = \rho^{\chi} \langle \mathbf{N} : \overrightarrow{\dot{\boldsymbol{\varepsilon}}} \rangle \tag{14}$$

$$m = m_R + (1 - m_R) y_h \tag{15}$$

whereby χ is an exponent controlling the shape of the stiffness degradation curve and m_R is the maximum stiffness factor considered as a parameter. The factor ρ^{χ} in Eq. (14) is aimed to reduce the plastic strain rate upon cyclic loading, while the second $\langle \mathbf{N} : \overrightarrow{\dot{\boldsymbol{\varepsilon}}} \rangle$ guarantees the continuity of the material response in the vicinity of the neutral loading [19]. Notice that these variables range between $1 \leq m \leq m_R$ and $0 \leq y_h \leq 1$. Hence, while the magnitudes $\bar{\mathsf{E}}$ and $\dot{\bar{\boldsymbol{\varepsilon}}}^{p}$ are adjusted to simulate the behavior at mobilized states, or equivalently, at medium or large strain amplitudes $\| \Delta\boldsymbol{\varepsilon} \| > 10^{-3}$, the factors m and y_h are responsible for the small strain effects.

Experiments on cyclic loading with a large number of repetitions ($N > 30$) have shown that the plastic accumulation rate reduces for increasing number of consecutive cycles when stress loops are performed away from the critical state line [58]. Poblete et al. [43] showed that this effect can be captured through the modification of the exponent χ (see Eq. 14). In order to do this, they introduced an additional state variable to distinguish whether the soil is performing a few or several consecutive cycles. The state variable, denoted with ε_a, evolves according to the relation:

$$\dot{\varepsilon}_a = \frac{C_a}{R}(1 - y_h - \varepsilon_a) \| \dot{\boldsymbol{\varepsilon}} \| \tag{16}$$

whereby C_a is a parameter controlling its rate. Hence, when $\varepsilon_a \approx 0$ means that a few cycles or monotonic loading has been recently performed, whereas $\varepsilon_a \to 1$ suggests that several consecutive cycles have been experienced. This information is accounted in the formulation of exponent χ which according to Poblete et al. [43] reads:

$$\chi = \chi_0 + \varepsilon_a(\chi_{\max} - \chi_0) \tag{17}$$

whereby χ_0 and $\chi_{\max}$ are material parameters. The first should be calibrated for a single cycle and the second after performing a number of consecutive cycles. The transition between these two states is controlled by parameter C_a. Their calibration has been previously explained in [43] but will be recapitulated in "Appendix." Notice that one may ignore this effect setting $C_a = 0$ and $\chi_0 = \chi_{\max}$.

Considering that the viscous strain rate $\dot{\boldsymbol{\varepsilon}}^{\text{vis}}$ is always active, an elastic step of the intergranular strain model, i.e., $F_{\text{H}} < 0$, produces a viscoelastic step on the mechanical model, $y_h = 0$. Under mobilized states $\rho = 1$, the scalar functions yield to $m = 1$ and $y_h = 1$ and the model (Eq. 11) turns into (visco-)hypoplastic. Table 1 summarizes the constitutive equation for the intergranular strain model and mechanical model according to the strain amplitude. The equations presented herein correspond to the general form of the mechanical model. In order to simulate a particular material, one should define the model for mobilized states. In order to do this, the definition of the magnitudes $\bar{\mathsf{E}}$, $\dot{\bar{\boldsymbol{\varepsilon}}}^{p}$ and $\dot{\boldsymbol{\varepsilon}}^{\text{vis}}$ are required. They are explained in the following section.

3 Constitutive model for clays under mobilized states

ISA-plasticity-based models require the definition of the magnitudes $\bar{\mathsf{E}}$, $\dot{\bar{\boldsymbol{\varepsilon}}}^{p}$ and $\dot{\boldsymbol{\varepsilon}}^{\text{vis}}$ to simulate the soil behavior under mobilized states $\rho = 1$. As mentioned before, one may choose relations of existing hypoplastic models for

Table 1 Summary of the model stages according to the current strain amplitude

Name	$\dot{\mathbf{h}}$	$\dot{\boldsymbol{\sigma}}$	m	y_h
Elastic[a]	$= \dot{\boldsymbol{\varepsilon}}$,	$= m_R\bar{\mathsf{E}} : (\dot{\boldsymbol{\varepsilon}} - \dot{\boldsymbol{\varepsilon}}^{\text{vis}})$	$= m_R$	$= 0$
Transition	$= \dot{\boldsymbol{\varepsilon}} - \dot{\lambda}\mathbf{N}$,	$= m\bar{\mathsf{E}} : (\dot{\boldsymbol{\varepsilon}} - y_h\dot{\bar{\boldsymbol{\varepsilon}}}^{p} - \dot{\boldsymbol{\varepsilon}}^{\text{vis}})$	> 1	< 1
Mobilized state	$= \mathbf{0}$,	$= \bar{\mathsf{E}} : (\dot{\boldsymbol{\varepsilon}} - \dot{\bar{\boldsymbol{\varepsilon}}}^{p} - \dot{\boldsymbol{\varepsilon}}^{\text{vis}})$	$= 1$	$= 1$

[a] More specifically, elastic for the intergranular strain model and viscoelastic for the mechanical model

clays for these magnitudes, e.g., [24, 34, 55]. For the proposed model, some relations proposed by [17] to simulate clays are adopted, while other functions are herein proposed. So far, an ISA model has never been formulated with the consideration of viscous effects. Therefore, a relation for the viscous strain rate $\dot{\boldsymbol{\varepsilon}}^{\mathrm{vis}}$ is also proposed and evaluated. These relations are explained in the subsequent lines.

The formulations of the magnitudes $\bar{\mathsf{E}}$ and $\dot{\bar{\boldsymbol{\varepsilon}}}^{p}$ are based on two characteristic void ratios corresponding to the maximum and critical state void ratio and denoted with $e_i = e_i(p)$ and $e_c = e_c(p)$, respectively. They follow from Modified Cam Clay (MCC) relations [45] and read:

$$\text{Maximum void ratio}: \quad \mathrm{e_i} = e_{i0} - \lambda \log(p/p_{\mathrm{ref}}) \tag{18}$$

$$\text{Critical state void ratio}: \quad \mathrm{e_c} = e_i - \lambda \log(2) \tag{19}$$

with the parameters e_{i0} and λ and the reference pressure of $p_{\mathrm{ref}} = 1$ kPa. Figure 3a illustrates an example of the curves describing e_c and e_i. Similarly, the model considers two characteristic stress surfaces, namely the critical and bounding state surface. The critical state surface presents the same definition as in classical models [45] and is described through the function F_c:

$$\text{Critical state surface}: \quad \mathrm{F_c} \equiv \| \mathbf{r} \| - \| \mathbf{r}_{\mathrm{c}} \| = 0,$$
$$\mathbf{r}_c = \sqrt{2/3} M_c g(\theta_{\mathbf{r}}) \overrightarrow{\mathbf{r}} \tag{20}$$

where $\mathbf{r} = \boldsymbol{\sigma}^*/p$ is the stress ratio tensor, $\boldsymbol{\sigma}^*$ is the stress deviator, $p = -\mathrm{tr}\boldsymbol{\sigma}/3$ is the mean stress, M_c is the slope of the critical state line CSL in the $p-q$ space under triaxial compression, and the scalar function $g = g(\theta_{\mathbf{r}})$ is a scalar function responsible for its shape in the deviator stress plane, as depicted in Fig. 3b. The function $g = g(\theta_{\mathbf{r}})$ depends on the Lodes angle $\theta_{\mathbf{r}}$ of the stress ratio $\mathbf{r}$ and ranges between $c \le g \le 1$, whereby $c = M_e/M_c = 3/(3 + M_c)$ represents the ratio between the critical state slope for triaxial extension M_e and triaxial compression M_c according to the Mohr–Coulomb relation. The scalar function $g = g(\theta)$ is taken from Argyris et al.[2] and reads:

$$g(\theta) = \frac{2c}{(1+c) - (1-c)\cos(3\theta)} \tag{21}$$

The bounding surface describes the state in which the plastic strain rate for mobilized states renders $\| \dot{\bar{\boldsymbol{\varepsilon}}}^{p} \| = \| \dot{\boldsymbol{\varepsilon}} \|$. As explained in [19], the position of this surface is close (but not equal) to the peak stress ratio obtained under monotonic triaxial shearing. For its description, we adopt the wedge-capped surface proposed by [19] described with the function $F_b = 0$. Figure 3c depicts the bounding surface $F_b = 0$ within the $p-q$ space. Notice the intersections in point A with the e_c curve and in point B with the e_i curve. The function F_b reads:

$$\text{Bounding surface}: \quad \mathrm{F_b} \equiv \| \mathbf{r} \| - \| \mathbf{r}_{\mathrm{b}} \| = 0$$
$$\text{with} \quad \mathbf{r}_{\mathrm{b}} = \mathbf{r}_{\mathrm{c}} \mathrm{f_b}$$
$$\text{and} \quad \mathrm{f_b} = \mathrm{f_{b0}} \left(1 - \left(\frac{\mathrm{e}}{\mathrm{e_i}} \right)^{\mathrm{n_F}} \right)^{1/2} \tag{22}$$

where $f_{b0} > 1$ is a material parameter defining the maximum norm $\| \mathbf{r} \|$ at the bounding surface and n_F is an exponent deduced to ensure the point at which the surface intersects the critical state line [19]:

$$n_F = \frac{\log\left(\left(f_{b0}^2 - 1 \right) / f_{b0}^2 \right)}{\log(e_c/e_i)} \tag{23}$$

The tensors $\mathbf{r}_b$ and $\mathbf{r}_c$ from Eqs. (22) and (20), respectively, are images of the stress ratio $\mathbf{r}$ at the bounding and critical state surface according to the mapping rule depicted in Fig. 3b. Having the characteristic stress surfaces and void ratios defined, it is proceeded with the definition of the magnitudes $\bar{\mathsf{E}}$, $\dot{\bar{\boldsymbol{\varepsilon}}}^{p}$ and $\dot{\boldsymbol{\varepsilon}}^{\mathrm{vis}}$. The elastic stiffness at mobilized states $\bar{\mathsf{E}}$ is adopted from [17] and reads:

$$\bar{\mathsf{E}} = 3\bar{K} \overrightarrow{\mathbf{1}} \overrightarrow{\mathbf{1}} + 2\bar{G} \left(\mathsf{I} - \overrightarrow{\mathbf{1}} \overrightarrow{\mathbf{1}} \right) - \frac{\bar{K}}{\sqrt{2}} (\mathbf{1r} + \mathbf{r1}) \tag{24}$$

whereby $\bar{K}$ and $\bar{G}$ are the bulk and shear modulus under mobilized states, I is the fourth-rank unit tensor for symmetric tensors $I_{ijkl} = 1/2(\delta_{ik}\delta_{jl} + \delta_{il}\delta_{jk})$, $\overrightarrow{\mathbf{1}} = \mathbf{1}/\sqrt{3}$ is the normalized Kronecker delta tensor, and $\mathbf{r} = \boldsymbol{\sigma}^*/p$ is the stress ratio. The bulk modulus $K = m\bar{K}$ and shear modulus $G = m\bar{G}$ are adjusted to the Modified Cam Clay (MCC) relations as follows:

$$\bar{K} = \frac{p}{\lambda} \frac{(1+e)}{(1-Y_{im})} \quad \text{with} \quad \mathrm{Y_{im}} = (\lambda - \kappa)/(\lambda + \kappa) \tag{25}$$

$$\bar{G} = \frac{(1-2\nu)}{2(1+\nu)} K \tag{26}$$

where ν is the Poisson ratio, and κ is the swelling index. The mobilized plastic strain rate tensor $\dot{\bar{\boldsymbol{\varepsilon}}}^{p}$ reads:

$$\dot{\bar{\boldsymbol{\varepsilon}}}^{p} = Y \mathbf{m} \| \dot{\boldsymbol{\varepsilon}} \| \tag{27}$$

whereby Y is the degree of non-linearity [37] and $\mathbf{m}$ is the flow rule adopted from [17]:

$$\mathbf{m} = \left[-1/2(\| \mathbf{r}_c \| - \| \mathbf{r} \|) + \frac{\mathbf{r}}{\| \mathbf{r}_c \|} \right]^{\rightarrow} \tag{28}$$

The degree of non-linearity Y is proposed with a similar interpolation function as in [37] and [35]:

$$Y = Y_i + (1 - Y_i) \left(\frac{\| \mathbf{r} \|}{\| \mathbf{r}_b \|} \right)^{n_Y} \quad \text{with} \quad \mathrm{Y_i} = \mathrm{Y_{im}} (\mathrm{p/p_i})^2 \tag{29}$$

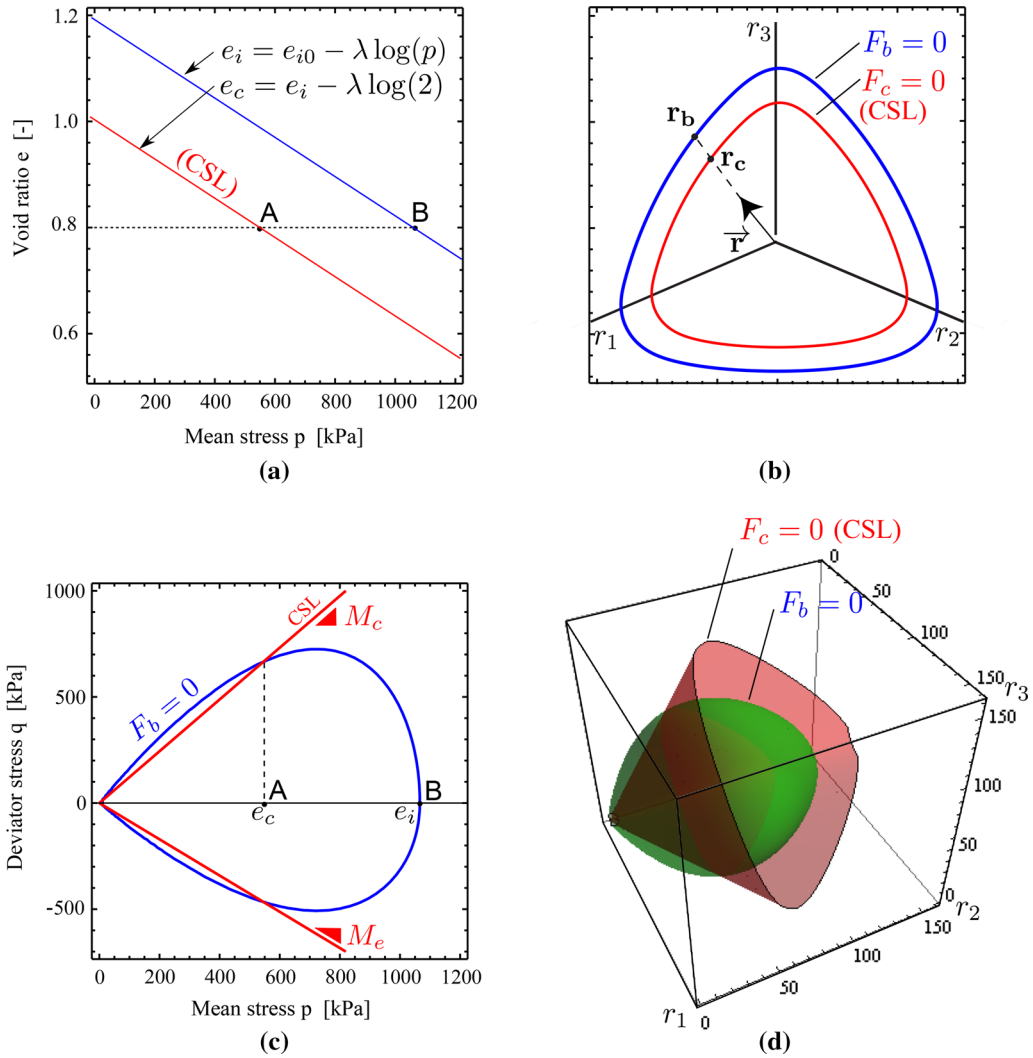

Fig. 3 Characteristic void ratios and stress surfaces. **a** Characteristic void ratios e_i and e_c. **b** Stress surfaces in the deviator plane. **c** Stress surfaces in the p–q plane. **d** Stress surfaces in the principal stress space

where the function $Y_i = Y_{im}(p/p_i)^2$, previously defined and analyzed in [18], has been adjusted to simulate the behavior at isotropic states $q = 0$, and $p_i = \exp((e_{i0} - e)/\lambda)$ is the Hvorslev mean stress representing the projection of p in the e_i curve for a given e. As explained in [20], higher values of n_Y would reduce the plastic strain rate for a given stress ratio $\mathbf{r}$. A minimum value of $n_Y = 2$ is recommended to assure a smooth response of the model around the isotropic stress axis $\mathbf{r} = \mathbf{0}$. We propose an exponent which increases with increasing number of consecutive cycles. Considering its similarity with the exponent χ, we propose the same interpolation function as in Eq. (17) but bounding the exponent between $2 \leq n_Y \leq \chi_{\max}$:

$$n_Y = 2 + \varepsilon_a(\chi_{\max} - 2) \tag{30}$$

4 Viscous strain rate $\dot{\boldsymbol{\varepsilon}}^{\text{vis}}$

The present section proposes a formulation for the viscous strain rate $\dot{\boldsymbol{\varepsilon}}^{\text{vis}}$ and discusses some aspects of the simulation of the strain rate dependency with the proposed relation. For the viscous strain rate $\dot{\boldsymbol{\varepsilon}}^{\text{vis}}$, the classical power relation widely used in several visco-plastic models [38, 40, 41, 50, 53] is herein adopted:

$$\dot{\boldsymbol{\varepsilon}}^{\text{vis}} = \frac{I_v}{\lambda}\left(\frac{1}{\text{OCR}_{3\text{D}}}\right)^{1/I_v}\mathbf{m} \tag{31}$$

whereby I_v is the viscosity index and $\text{OCR}_{3\text{D}}$ is the definition of overconsolidation ratio for 3D states. Detailed analysis of this relation can be found in [37, 40, 53]. For $I_v = 0$ we set $\dot{\boldsymbol{\varepsilon}}^{\text{vis}} = \mathbf{0}$ avoiding the exponent discontinuity. Similar to Vermeer [53] and Niemunis [37], a three-

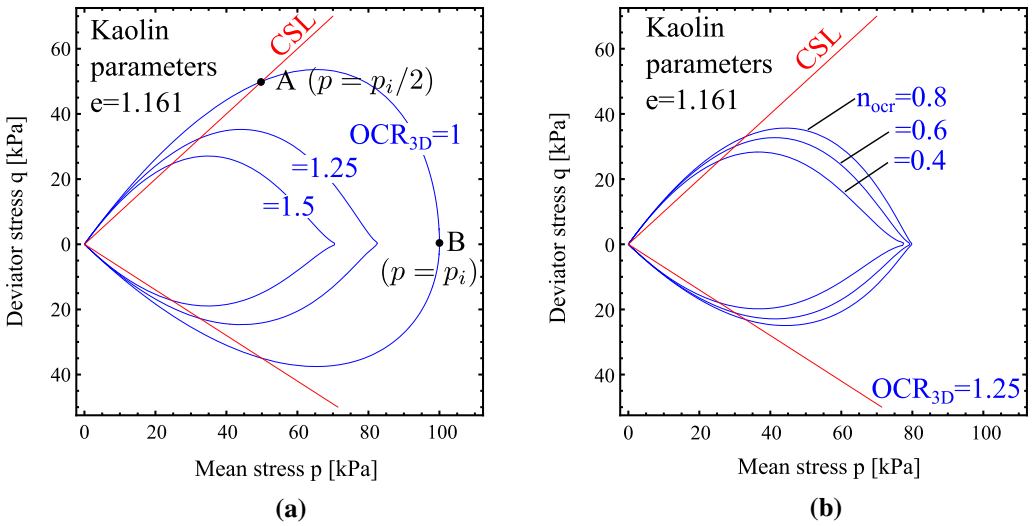

Fig. 4 Shape of the OCR_{3d} surface (Eq. 32) with Kaolin parameters. **a** Variation of the value of OCR_{3D}. **b** Variation of parameter n_{OCR} with $OCR_{3D} = 1.25$

dimensional definition of the overconsolidation ratio is required. This is usually formulated as a surface within the stress space. Of course, a capped surface would be the most appropriate for this purpose. For the sake of consistency, the surface must intersect the isotropic stress axis at $OCR_{3D} = p_i/p$ (for $q = 0$). We propose a similar function as the one used in the degree of non-linearity considering its simplicity (see Eq. 29):

$$OCR_{3D} = \frac{p_i}{p} + \left(1 - \frac{p_i}{p}\right)\left(\frac{\| \mathbf{r} \|}{\| \mathbf{r}_b \|}\right)^{n_{ocr}} \tag{32}$$

where n_{ocr} is an additional parameter to control the shape of the surface. Figure 4 shows the shape of the proposed surface with the variation of OCR_{3D} and the parameter n_{ocr}. As one may note, under isotropic stress states the relation $OCR_{3D} = p_i/p$ holds and one recovers the one-dimensional definition of the overconsolidation ratio. For the condition $OCR_{3D} = 1$, the surface coincides with the bounding surface $F_b = 0$; see Fig. 4a. Therefore, it intercepts the critical state surface at $p = p_i/2$; see point A. For higher $OCR_{3D} > 1$, the size of the surface reduces and its shape is controlled by the parameter n_{ocr}; see Fig. 4b. Lower values of n_{ocr} produce a narrower shape of the surface. This effect will allow to calibrate the parameter n_{ocr} using undrained triaxial tests as described in "Appendix."

Some illustrative simulations are given in Fig. 5 to understand the model performance when dealing with time-dependent effects. For instance, the simulations borrow the parameters of the Kaolin clay from Table 1. In Fig. 5a the simulation of isotropic compression paths presenting different strain rate is shown. These compression paths are also known as isotachs, and their position depends on the strain rate. The simulation shows that the maximum void ratio curve $e = e_i$ is only reachable under infinite strain rate, similar as in other formulations [6, 27, 61]. Under undrained triaxial shearing, slower strain rates return a higher pore water pressure development; see Fig. 5b.

All these relations define the proposed model. Notice that one may simplify the constitutive model to different formulations according to the problem of interest. For example, for elastic problems, one may set $I_v = 0$ and $R \to \infty$ which reduces the model to $\dot{\boldsymbol{\sigma}} = m_R \bar{E} : \dot{\boldsymbol{\varepsilon}}$. For models specializing on monotonic loading without viscous effects, one may use the assumptions $R \to 0$ and $I_v = 0$ which reduces to the hypoplastic model $\dot{\boldsymbol{\sigma}} = \bar{E} : (\dot{\boldsymbol{\varepsilon}} - \dot{\bar{\boldsymbol{\varepsilon}}}^p)$. Under the same assumptions, one may consider the strain rate dependency with $I_v > 0$ which results in the equation $\dot{\boldsymbol{\sigma}} = \bar{E} : (\dot{\boldsymbol{\varepsilon}} - \dot{\bar{\boldsymbol{\varepsilon}}}^p - \dot{\boldsymbol{\varepsilon}}^{vis})$, and finally a model consistent with a wide range of strain amplitudes and considering viscous effects is $\dot{\boldsymbol{\sigma}} = m\bar{E} : (\dot{\boldsymbol{\varepsilon}} - y_h \dot{\bar{\boldsymbol{\varepsilon}}}^p - \dot{\boldsymbol{\varepsilon}}^{vis})$. Table 2 presents a summary of the different forms which can be obtained from the simplification of the proposed model given some assumptions.

Summary of constitutive relations

Constitutive equation:

$$\dot{\boldsymbol{\sigma}} = m\bar{E} : (\dot{\boldsymbol{\varepsilon}} - y_h \dot{\bar{\boldsymbol{\varepsilon}}}^{p} - \dot{\boldsymbol{\varepsilon}}^{\mathrm{vis}})$$

with the scalar functions according to ISA-plasticity:

$m = m_R + (1 - m_R) y_h$ (Function to increase stiffness upon cycles)

$y_h = \rho^{\chi} \langle \mathbf{N} : \overrightarrow{\dot{\boldsymbol{\varepsilon}}} \rangle$ (Function to reduce plastic strain rate upon cycles)

$\chi = \chi_0 + \varepsilon_a(\chi_{\max} - \chi_0)$ (Exponent of the intergranular strain effect)

Relations for mobilized states $y_h = 1$:

$$\bar{\mathsf{E}} = 3\bar{K}\,\overrightarrow{\mathbf{1}}\,\overrightarrow{\mathbf{1}} + 2\bar{G}\left(\mathsf{I} - \overrightarrow{\mathbf{1}}\,\overrightarrow{\mathbf{1}}\right) - \frac{\bar{K}}{\sqrt{2}}(\mathbf{1r} + \mathbf{r1})$$ (Eq. 25 for $\bar{K}$ and Eq. (26) for $\bar{G}$)

$\dot{\bar{\boldsymbol{\varepsilon}}}^{p} = Y\mathbf{m} \parallel \dot{\boldsymbol{\varepsilon}} \parallel$ (Mobilized plastic strain rate)

$Y = Y_i + (1 - Y_i)\left(\frac{\parallel \mathbf{r} \parallel}{\parallel \mathbf{r}_b \parallel}\right)^{n_Y}$ with $\mathrm{Y_i} = \mathrm{Y_{im}(p/p_i)^2}$ (Eq. 22 for $\mathbf{r}_b$ and Eq. 30 for n_Y)

$$\mathbf{m} = \left[-1/2(\parallel \mathbf{r}_c \parallel - \parallel \mathbf{r} \parallel) + \frac{\mathbf{r}}{\parallel \mathbf{r}_c \parallel}\right]^{\rightarrow}$$ (Flow rule, Eq. 20 for $\mathbf{r}_c$)

$$\dot{\boldsymbol{\varepsilon}}^{\mathrm{vis}} = \frac{I_v}{\lambda}\left(\frac{1}{\mathrm{OCR_{3D}}}\right)^{1/I_v}\mathbf{m}$$ (Viscous strain rate)

$$\mathrm{OCR_{3D}} = \frac{p_i}{p} + \left(1 - \frac{p_i}{p}\right)\left(\frac{\parallel \mathbf{r} \parallel}{\parallel \mathbf{r}_b \parallel}\right)^{n_{\mathrm{ocr}}}$$ (3D definition of overconsolidation ratio)

Yield surface

$$F_H = \parallel \mathbf{h} - \mathbf{c} \parallel - \frac{R}{2}$$ (Yield surface of the model)

Intergranular strain model

$\dot{\mathbf{h}} = \dot{\boldsymbol{\varepsilon}} - \dot{\lambda}_H \mathbf{N}$ (Intergranular strain rate, with $\mathbf{N} = (\mathbf{h} - \mathbf{c})^{\rightarrow}$, Eq. 9 for $\dot{\lambda}_H$)

$\dot{\mathbf{c}} = \dot{\lambda}_H \beta_h (\mathbf{c}_b - \mathbf{c})/R$ (Back-Intergranular strain rate, with $\mathbf{c}_b = (R/2)\overrightarrow{\dot{\boldsymbol{\varepsilon}}}$)

$\dot{\varepsilon}_a = \frac{C_a}{R}(1 - y_h - \varepsilon_a) \parallel \dot{\boldsymbol{\varepsilon}} \parallel$ (Evolution of internal variable for cyclic history)

5 Numerical implementation and parameters

The proposed model has been implemented with the programming language FORTRAN, as a material subroutine from the commercial finite element software ABAQUS standard. The classic "elastic predictor" scheme has been followed to perform the numerical implementation [48]. A substepping scheme with small strain increments has been implemented to guarantee numerical convergence. All the terms except the viscous strain rate were explicitly implemented (evaluated at the beginning of the subincrement). For the viscous strain rate, a semi-implicit scheme has been implemented following a similar integration scheme as by Niemunis [37].

The proposed model requires the calibration of 14 parameters. They are subdivided into different groups according to their role within the model, namely "Elasticity" (ν, κ, λ), "Plasticity" (e_{i0}, M_c, f_{b0}), "Viscosity" (I_v, n_{ocr}) and "Intergranular strain" (m_R, R, β, χ_0, $\chi_{\max}$, C_a). All parameters except for n_{ocr} have been already used in former works, e.g., [17, 19, 40, 43] and detailed in [22], but their calibration are once more explained in "Appendix."

6 Simulations with experiments

We evaluate the performance of the proposed model through the simulation of the experimental results of two different clays, namely the Kaolin Clay and the Lower Rhine clay. Table 4 provides an overview of the index properties of these clays, including the liquid limit w_L, plastic limit w_P, plasticity index I_P and grain density ρ_s [57]. The set of experiments includes oedometric and triaxial tests under several conditions, such as monotonic and cyclic loading and with the variation of the strain velocity. In all simulations the intergranular strain $\mathbf{h}$ and the back-intergranular strain have been initialized with $\mathbf{h} = -R\overrightarrow{\mathbf{1}}$ and $\mathbf{c} = \mathbf{h}/2$ which corresponds to a fully mobilized state after isotropic compression. This would represent the initial isotropic consolidation of the sample before performing the test. The parameter calibration of both materials has been performed following the short guide from Sect. 1. Table 3 lists the selected parameters for these materials.

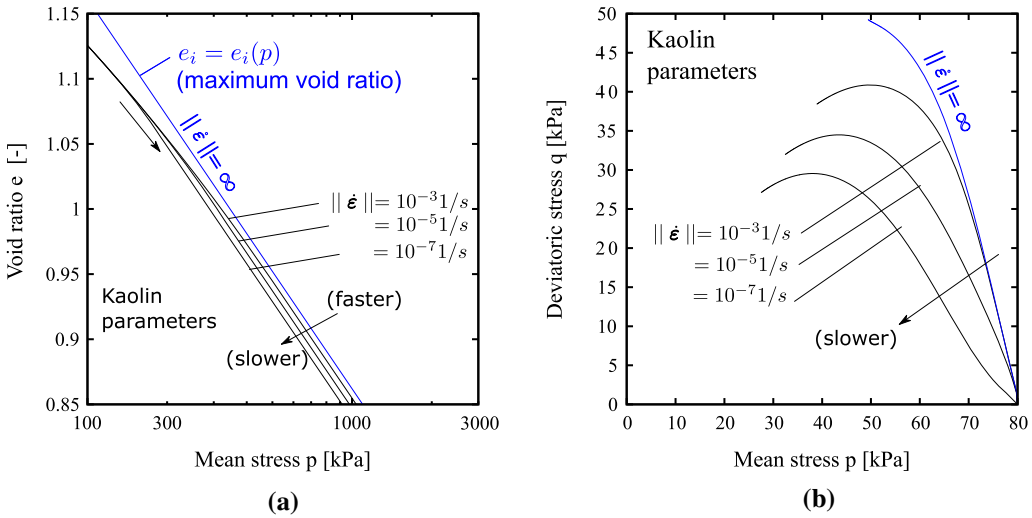

Fig. 5 Simulations with different strain rates (isotachs). **a** Isotropic compression. **b** Undrained triaxial test

Table 2 Simplification of the general constitutive model to some particular forms

Name	Assumptions	Simplified equation
Elastic	$R \to \infty$, $I_v = 0$	$\dot{\boldsymbol{\sigma}} = m_R \bar{E} : \dot{\boldsymbol{\varepsilon}}$.
Viscoelastic	$R \to \infty$	$\dot{\boldsymbol{\sigma}} = m_R \bar{E} : (\dot{\boldsymbol{\varepsilon}} - \dot{\boldsymbol{\varepsilon}}^{\text{vis}})$.
Hypoplastic	$R \to 0$, $I_v = 0$	$\dot{\boldsymbol{\sigma}} = \bar{E} : (\dot{\boldsymbol{\varepsilon}} - \dot{\bar{\boldsymbol{\varepsilon}}}^{p})$
Visco-hypoplastic	$R \to 0$	$\dot{\boldsymbol{\sigma}} = \bar{E} : (\dot{\boldsymbol{\varepsilon}} - \dot{\bar{\boldsymbol{\varepsilon}}}^{p} - \dot{\boldsymbol{\varepsilon}}^{\text{vis}})$
ISA-plasticity	None	$\dot{\boldsymbol{\sigma}} = mE : (\dot{\boldsymbol{\varepsilon}} - y_h \dot{\boldsymbol{\varepsilon}}^{p} - \dot{\boldsymbol{\varepsilon}}^{\text{vis}})$

6.1 Simulations with Kaolin clay

The Kaolin is a medium plasticity clay with a viscosity index equal to $I_v = 0.015$. Reconstituted samples of height and diameter equal to 50 mm were used for this purpose. Figure 6 shows the first experiment and corresponds to an oedometer test showing time-dependent effects. The experiment consists on several stages with different strain rates and creep phases. It includes also some unloading-reloading cycles showing hysteretic behavior. All these

Table 3 Material parameters of the proposed model

Description		Units	Approx. range	Kaolin	Lower Rhine clay
Elasticity					
λ	Compression index	[–]	10^{-6}–1	0.13	0.26
κ	Swelling index	[–]	10^{-6}–1	0.05	0.04
ν	Poisson ratio	[–]	0–0.5	0.33	0.2
Plasticity					
e_{i0}	Maximum void ratio at $p = p_{\text{ref}}$	[–]	0.5–2	1.76	2.47
M_c	CS slope	[–]	0.5–1.5	1.0	0.95
f_{b0}	Bounding surface factor	[–]	1–2	1.1	1.45
Viscosity					
I_v	Viscosity index	[–]	1–2	0.015	0.025
n_{ocr}	Viscous exponent	[–]	0.4–2.0	0.4	0.5
Intergranular strain					
m_R	Stiffness factor	[–]	1–7	5	5
R	IS yield surface radius	[–]	10^{-5}–10^{-4}	2×10^{-4}	10^{-4}
β	IS hardening parameter	[–]	0–1	0.076	0.2
χ_0	Minimum IS exponent	[–]	1–10	7	7
χ_{max}	Maximum IS exponent	[–]	20–50	40	7
C_a	Accumulation rate factor	[–]	0–0.1	0.005	0

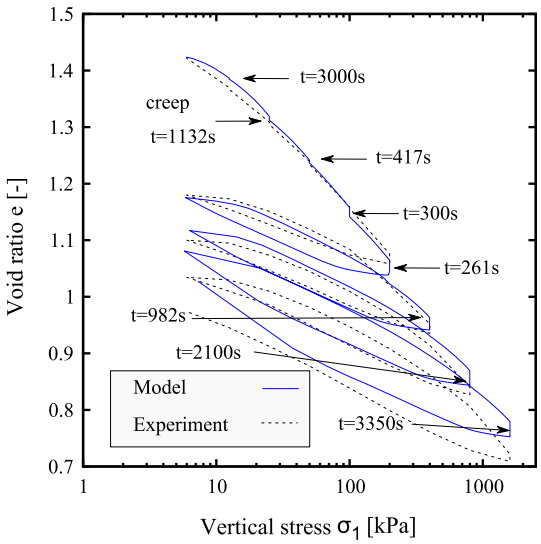

Fig. 6 Oedometer test with loading, unloading-reloading and creep steps

observations were captured by the proposed model which is also shown in the same figure.

Figure 7 shows a set of undrained triaxial tests with the Kaolin clay. All these experiments were conducted with a constant axial strain rate equal to $\dot{\varepsilon}_1 = 10^{-8}$ 1 / s, except for the last experiment in Fig. 7e, f whereby a sequence of different strain rates has been applied. Figure 7a, b shows the results of three normal consolidated samples with different confining pressures $p_0 = \{100, 200, 300\}$ kPa. The simulations captured fairly well most of the observed behavior with some discrepancies with respect to the peak stress. Figure 7c, d shows the results with overconsolidated samples. All samples were initially preloaded under isotropic compression and subsequently unloaded till reaching the desired stress and overconsolidation ratio (OCR). At this stage, overconsolidation ratios equal to OCR $= \{2, 4, 8\}$ were reached by the different samples. Simulations show also a similar pattern with the peak stress (Fig. 7c) although the behavior on the $p - q$ plane seems to be in agreement (Fig. 7d). The last experiment shown in Fig. 7e, f includes the variation of the vertical strain rate according to the following sequence: $\dot{\varepsilon} = 10^{-4} \rightarrow 10^{-5} \rightarrow 10^{-6} \rightarrow 10^{-5}$ 1 / s. Some strain rate "jumps" are of course evidenced in the results, which are also captured by the model. Simulation of this test gave satisfactory results.

The performance of the model on cyclic loading is evaluated with the subsequent experiments. They correspond to cyclic undrained triaxial tests having different deviator stress amplitudes q^{amp}. All cycles are symmetric with respect to the isotropic stress axis. The experiments present a deviator stress amplitude of $q^{\text{amp}} = 70$, 50 and 40 kPa and are shown in Figs. 8, 9 and 10, respectively. They initiated with a confining pressure of $p_0 = 200$ kPa. Considering their different stress amplitudes q^{amp}, they differed on the number of cycles N to reach failure, with $N \approx 6$ for $q^{\text{amp}} = 70$ kPa, $N \approx 35$ for $q^{\text{amp}} = 50$ kPa and $N \approx 450$ for $q^{\text{amp}} = 40$ kPa. They all present a constant vertical strain rate of $\varepsilon_1 = 8 \times 10^{-5}$ 1 / s. Simulations were performed to analyze the model performance. The simulations showed in general an agreement with the observed behavior, especially with the amplitudes $q^{\text{amp}} = 70$ kPa and $q^{\text{amp}} = 50$ kPa. The accumulation of the pore water pressure p_w was fairly well reproduced.

6.2 Simulations Lower Rhine clay

The simulations with Lower Rhine Clay are within this section presented. The experimental results are taken from [57]. All samples are reconstituted and present a height and diameter equal to 54 mm. The selected parameters for the proposed model are given in Table 1. The extension by Poblete et al. [43] is not considered on the present simulations due to the lack of experiments with a large number of repetitive cycles. Therefore, we set $C_a = 0$ and $\chi_{\max} = \chi_0$.

An oedometer test presenting an unloading-reloading cycle is satisfactorily simulated by the proposed model, as shown in Fig. 11. In this particular test, no time-dependent effects were considered, and instead, the whole tests were conducted with a constant strain rate of $\dot{\varepsilon}_1 = 1.5 \times 10^{-6}$. The next simulations correspond to undrained triaxial tests and are shown in Fig. 12. Figure 12a, b shows the undrained shearing of two normal consolidated samples under different confining pressures $p_o = \{200, 400\}$ kPa, while Fig. 12c, d shows an undrained test considering the variation of the strain rate at different stages. The strain rate for Test 1 (see Fig. 12c, d) follows the sequence $\dot{\varepsilon}_1 = 10^{-6} \rightarrow 10^{-7} \rightarrow 10^{-6} \rightarrow 10^{-5} \rightarrow 10^{-6} \rightarrow 10^{-5} \rightarrow 10^{-6}$, while the second follows $10^{-6} \rightarrow 10^{-7} \rightarrow 10^{-6} \rightarrow 10^{-5} \rightarrow 5 \times 10^{-5}$. The simulations show a good agreement with the observed time-dependent effects.

7 Closure

In the present work a constitutive model for the simulation of saturated clays has been proposed. The model presents some interesting capabilities, such as the simulation of the strain rate dependency and the incorporation of small strain

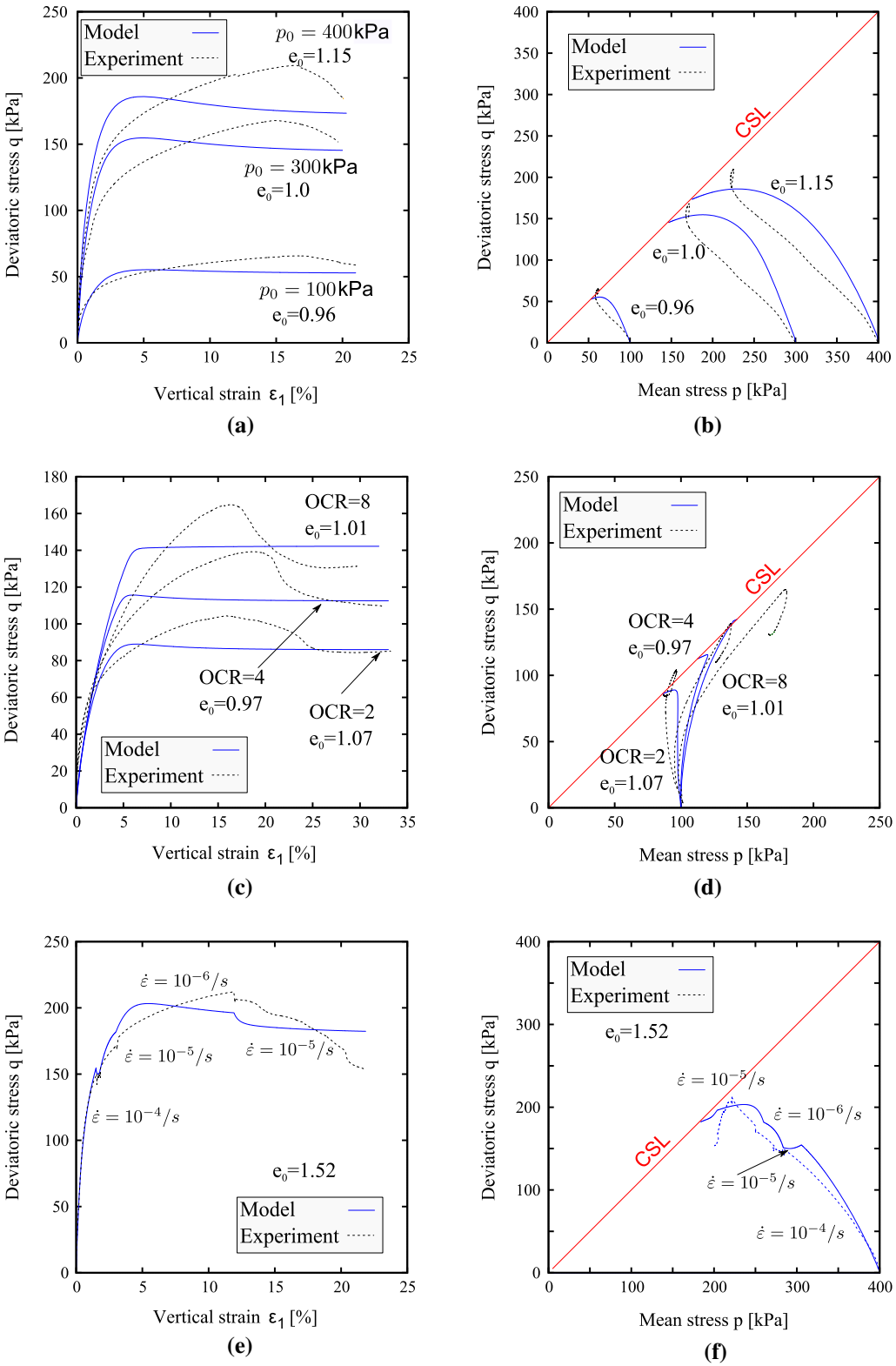

Fig. 7 Undrained triaxial tests. Kaolin clay

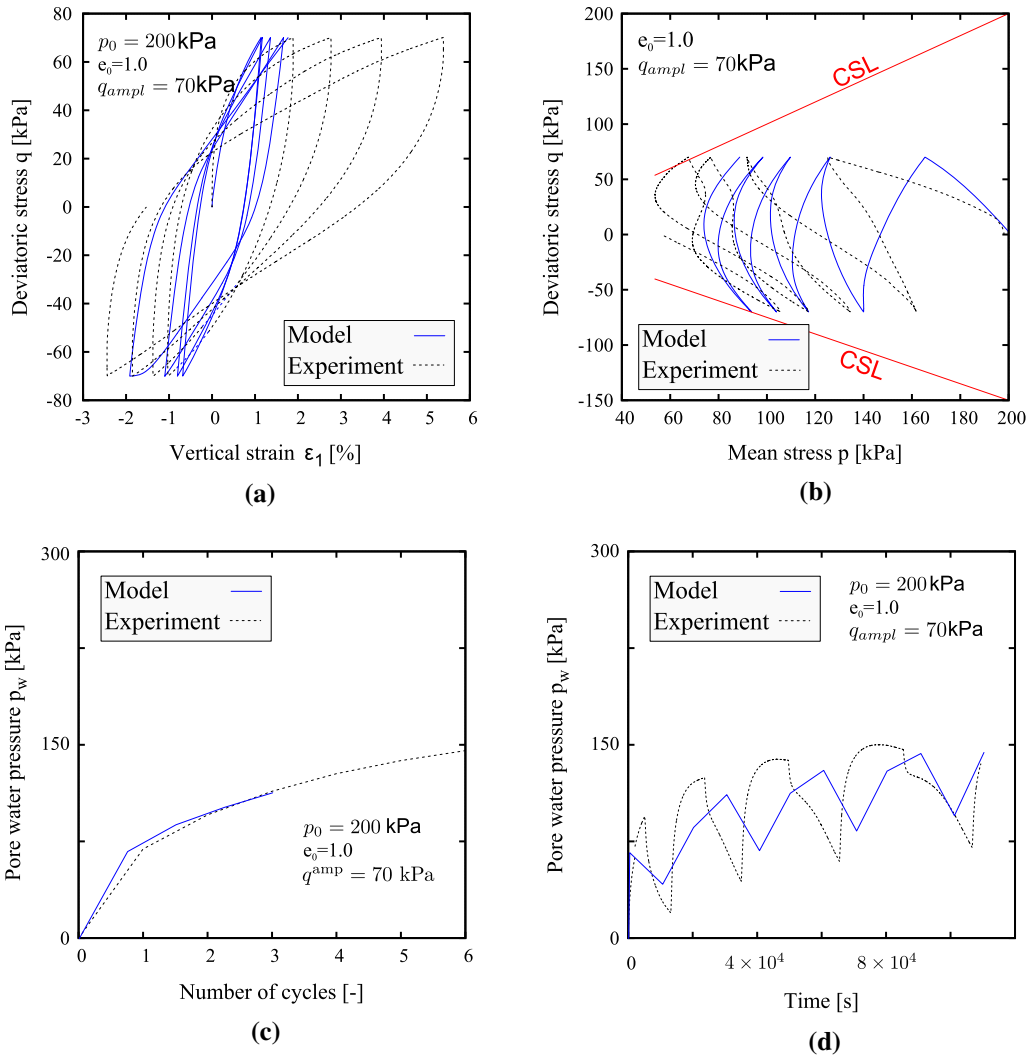

Fig. 8 Cyclic undrained triaxial tests with $q^{amp} = 70$ kPa. Kaolin clay. **a** q versus ε_1 space, **b** p versus q space, **c** experiment in p_w versus N space, **d** experiment in p_w versus t space

effects. Its formulation has been carefully proposed for a wide range of strain amplitudes without loosing generality of the model formulation. Of course, the complexity of the model formulation is high, but under some specific assumptions, it reduces to different types of constitutive formulations which are simpler to understand, such as Elasticity, Visco-Elasticity, Hypoplasticity and Visco-hypoplasticity; see Table 2. From the point of the constitutive

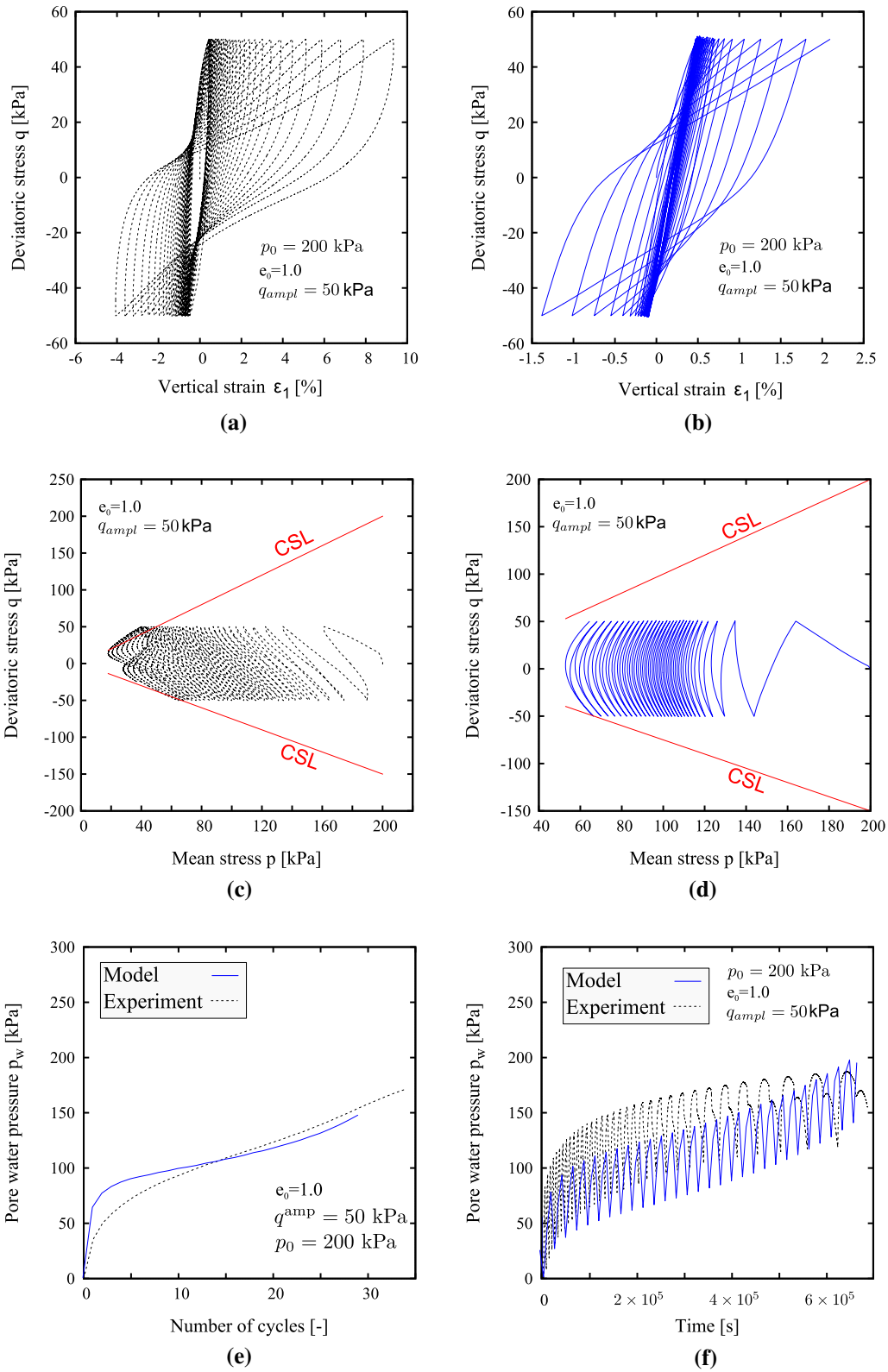

Fig. 9 Cyclic undrained triaxial tests with $q^{amp} = 50$ kPa. Kaolin clay. **a** Experiment in q versus ε_1 space, **b** simulation in q versus ε_1 space, **c** experiment in p versus q space, **d** simulation in p versus q space, **e** experiment in p_w versus N space, **f** experiment in p_w versus t space

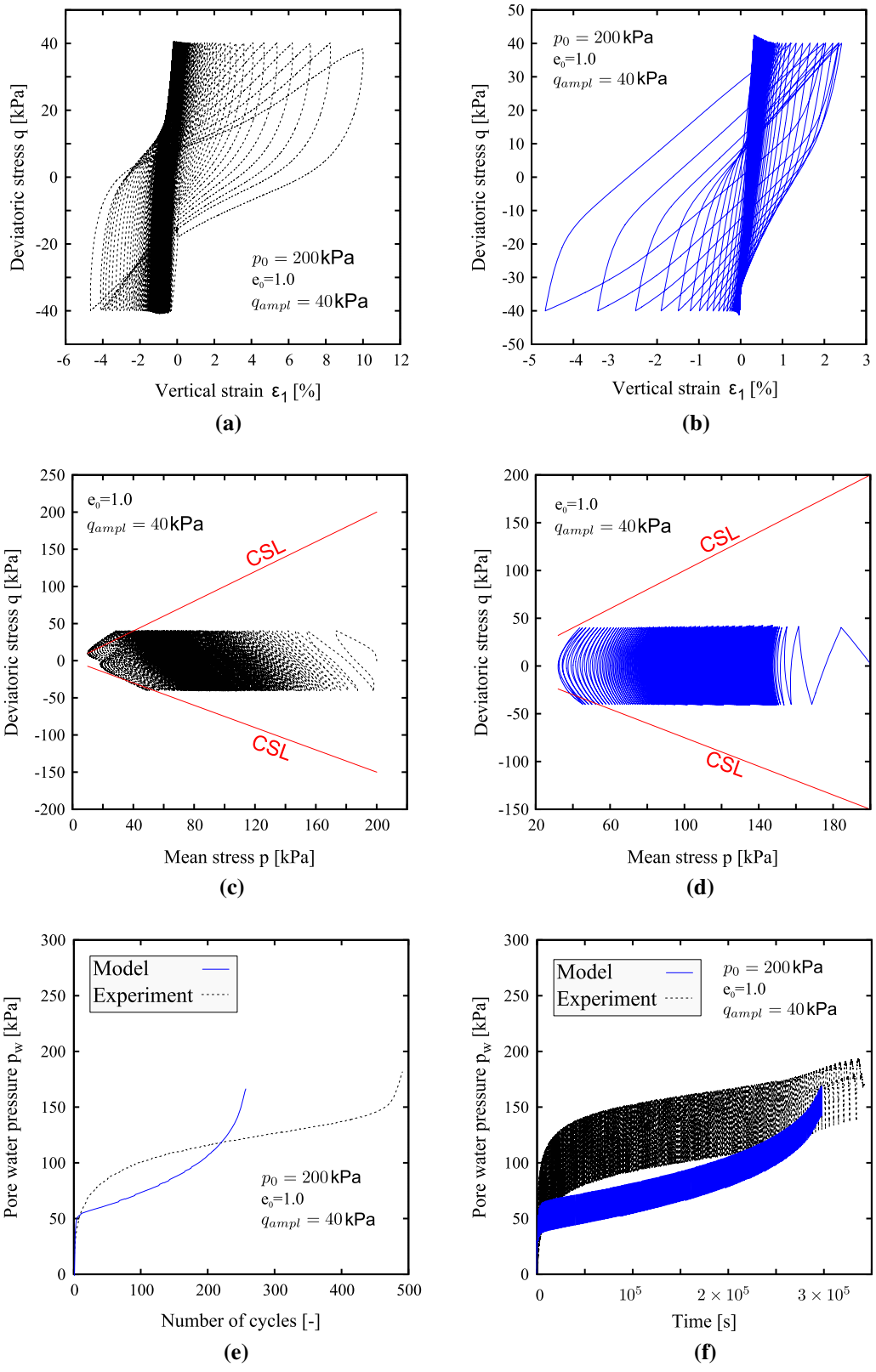

Fig. 10 Cyclic undrained triaxial tests with $q^{amp} = 40$ kPa. Kaolin clay. **a** experiment in q versus ε_1 space, **b** simulation in q versus ε_1 space, **c** experiment in p versus q space, **d** simulation in p versus q space, **e** experiment in p_w versus N space, **f** experiment in p_w versus t space

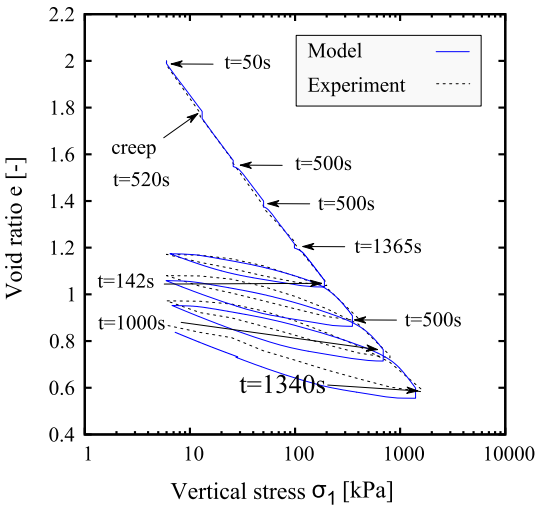

Fig. 11 Oedometer test with loading, unloading–reloading and creep steps. Lower Rhine clay

Table 4 Index properties of Kaolin clay and the Lower Rhine clay

Material	w_L[%]	w_P[%]	I_P[%]	$\rho_s[g/cm^3]$
Kaolin clay	47.2	35	12.2	2.675
Lower Rhine clay	56.1	22.0	34	2.59

modeling, this is very interesting because it permits the user to evaluate the influence of each effect on a simulation, such as viscosity or small strain effects, without changing the model and keeping the same set of material parameters. The simulations with some viscous clays have shown that the model is able to catch many aspects observed in these reconstituted clays. Some others experimental observations are left out for improvement in future works, such as the inherent anisotropy, cementation and partially saturation.

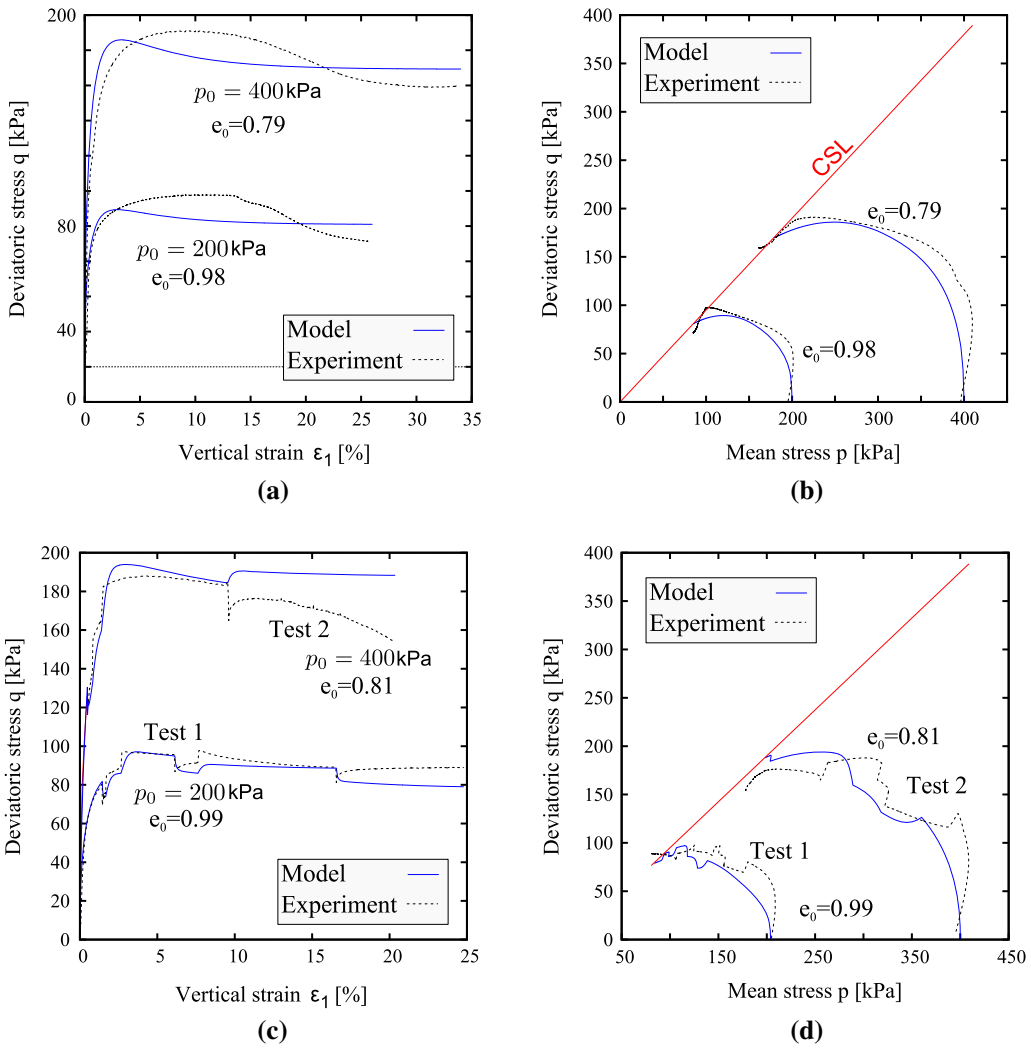

Fig. 12 Undrained triaxial tests on normal consolidated samples. Lower Rhine clay

Appendix

Short guide for the material parameter determination

The compression and swelling index, denoted with λ and κ, respectively, are calibrated with isotropic or oedometric compression tests. These parameters are computed in the e vs. $\log(p)$ space. As shown in Fig. 13, a compression path with constant strain rate is expected to approach asymptotically to a line with slope equal to λ. Hence, the measurement of this slope enables us to compute parameter λ. Parameter κ is calibrated instead upon an unloading path. In contrast to classical elastoplastic models, the proposed model delivers a hysteresis when simulating an unloading-reloading cycle. This implies that the slope during the cycle is not constant and is actually influenced by small strain effects. At the beginning of the unloading path, the simulation shows a slope equal to κ/m_R, whereby m_R is the factor responsible for the stiffness increase due to reversal loading (see Table 1). Subsequently, the small strain effects vanish and the simulation exhibits a slope similar to κ. Therefore, one may calibrate parameters κ and m_R with an unloading-reloading cycle.

The reference void ratio e_{i0} corresponds to the maximum void ratio at the reference pressure $p = 1$ kPa. The interpretation of e_{i0} is actually different as in other formulations considering the fact that the strain rate is decomposed into three components. According to the proposed model, the maximum void ratio curve $e = e_i(p)$ is only reached under infinite strain rate $\| \dot{\boldsymbol{\varepsilon}} \| = \infty$; see Fig. 3a. A sample compressed with infinite strain rate $\| \dot{\boldsymbol{\varepsilon}} \| = \infty$ is not feasible from the experimental point of view, and therefore, an alternative calibration method must be followed. For this purpose, the constitutive equation for an isotropic compression test under mobilized states is examined: By performing the operation $\dot{p} = -(\mathbf{1} : \dot{\boldsymbol{\sigma}})/3$, the constitutive equation reduces under mobilized states to (see Table 1):

$$\dot{p} = \bar{K}\left(\dot{\varepsilon}_v - Y_0\left(\frac{1}{\mathrm{OCR}}\right)^2 \mid \dot{\varepsilon}_v \mid -I_v/\lambda\left(\frac{1}{\mathrm{OCR}}\right)^{1/I_v}\sqrt{3}\right) \tag{33}$$

whereby $\mathrm{OCR} = p_i/p$ corresponds to the overconsolidation ratio for isotropic compression ($q = 0$) and $\dot{\varepsilon}_v = -\mathbf{1} : \dot{\boldsymbol{\varepsilon}}$ is the volumetric strain rate. On the other hand, an isotropic compression path with slope equal to λ can be also described with the non-viscous version of the model by setting $\mathrm{OCR} = 1$ and $I_v = 0$:

$$\dot{p} = \bar{K}(1 - Y_0)\dot{\varepsilon}_v \tag{34}$$

It is desired to find a simplified relation for compression paths under isotropic compression with the reference velocity $\dot{\varepsilon}_v = D_r$. The velocity D_r can be arbitrarily selected to match a particular experiment. Similar to Niemunis [37], this particular compression path is termed "Reference isotach." We recall that the maximum void ratio line $e_i = e_i(p)$ presents an overconsolidation ratio of $\mathrm{OCR} = 1$, and a different value is expected for the reference isotach. Let us denote the overconsolidation ratio for the reference isotach with $\mathrm{OCR}_{(\mathrm{ri})}$. By combining Eqs. (33) and (34) and setting $\dot{\varepsilon}_v = D_r$ and $\mathrm{OCR} = \mathrm{OCR}_{(\mathrm{ri})}$ yields to:

$$\begin{aligned}(1 - Y_0)D_{(\mathrm{ri})} = D_{(\mathrm{ri})} - Y_0\left(\frac{1}{\mathrm{OCR}_{(\mathrm{ri})}}\right)^2 D_{(\mathrm{ri})} \\ - I_v/\lambda\left(\frac{1}{\mathrm{OCR\ (ri)}}\right)^{1/I_v}\sqrt{3}\end{aligned} \tag{35}$$

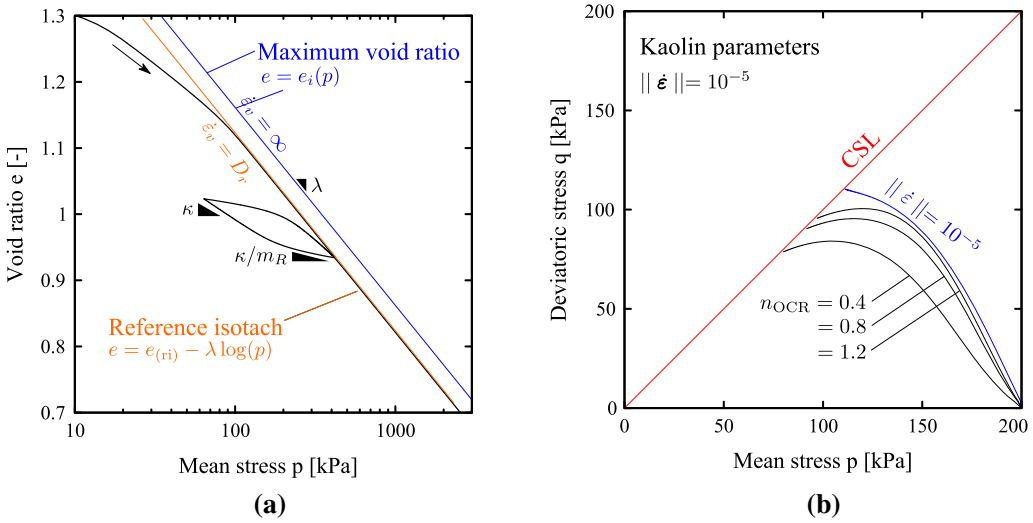

Fig. 13 Calibration of parameters. **a** Isotropic test. **b** Undrained triaxial test

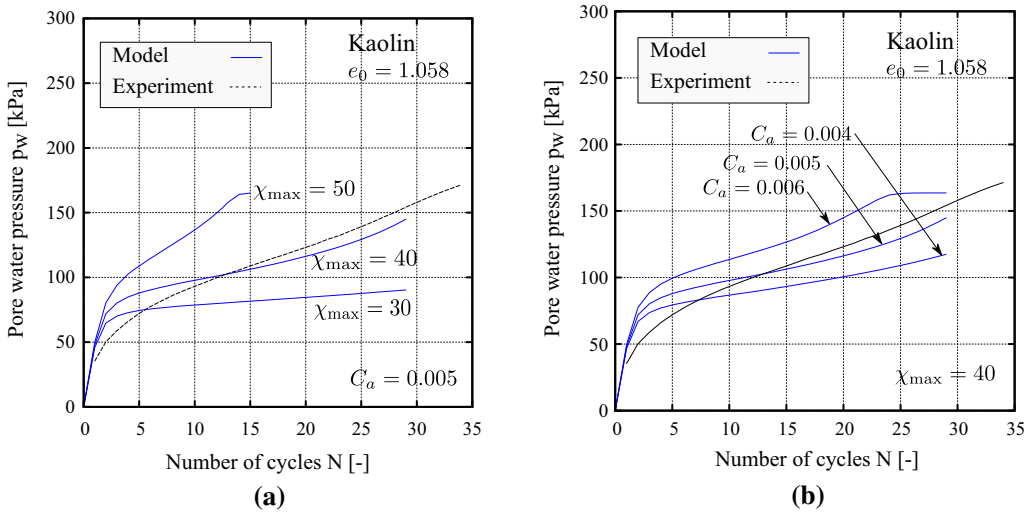

Fig. 14 Calibration of parameters χ_{max} and C_a using a cyclic undrained triaxial test with Kaolin

which can be numerically solved for $OCR_{(ri)}$. After solving this equation, one may compute e_{i0} from the relation:

$$e_{i0} = e_{(ri)} - \lambda \log(OCR_{(ri)}) \tag{36}$$

whereby $e_{(ri)}$ is the void ratio at $p = 1$ kPa at the reference isotach, which must be extrapolated from the experimental curve; see Fig. 13a. When only oedometric compression tests are performed, we suggest to use the same relations as an approximation taking advantage that the behavior is similar. The Poisson ratio v can be determined by measuring the shear modulus G for small strain amplitudes. An undrained triaxial test or a resonant column is useful for this purpose. If the shear modulus $G = G(p, e)$ for a given mean stress p and void ratio e is known, one can compute the bulk modulus $K = m_R \bar{K}$ according to Eq. (25) and solve for v from $r = G/K = 3(1 - 2v)/(2(1 + v))$. Notice that its determination depends on parameter m_R, which must be previously determined.

The slope of the critical state M_c is adjusted to the critical state line CSL. It corresponds to the slope within the $p - q$ space under triaxial compression. Points lying with vertical deformation of about $\varepsilon_1 > 20\%$ are recommended for its calibration. The parameter f_{b0} controls approximately the maximum stress ratio for triaxial compression $f_{b0} = \eta_{max}/M_c$. It can be adjusted to highly overconsolidated samples $OCR > 2$. When data are scarce, a recommended value of $f_{b0} = 1.3$ may be carefully used according to our experience with some clays. Of course, some simulations would help to check this recommendation.

The viscosity index I_v controls the intensity of the strain rate dependency. In this sense, an increasing value of I_v would return a larger creep deformation or increase the distance between the isotachs. The power relation used for the formulation of the viscous strain rate $\dot{\boldsymbol{\varepsilon}}^{vis}$, see Eq. (31), has been actually examined by many authors in former works [37, 53, 61]. In particular, Niemunis [37] showed that the viscosity index I_v of this formulation can be adjusted with compression curves of different strain rates (isotachs) with the following method: Consider two different isotachs with strain rate equal to $\|\underline{\boldsymbol{\varepsilon}}_a\|$ and $\|\underline{\boldsymbol{\varepsilon}}_b\|$ and overconsolidation ratio of OCR_a and OCR_b, respectively. Niemunis showed that for Eq. (31), the following relation, previously proposed by Leinenkugel [31], also holds:

$$I_v = \ln\left(\frac{OCR_b}{OCR_a}\right) / \ln\left(\frac{\|\underline{\boldsymbol{\varepsilon}}_a\|}{\|\underline{\boldsymbol{\varepsilon}}_b\|}\right) \tag{37}$$

Parameter n_{ocr} controls the shape of the OCR_{3D} surface (see Fig. 4b) and therefore the viscous effects under stress states different than the isotropic $q \neq 0$. As shown in Fig. 13b, an increasing value of n_{ocr} delivers a lower excess of pore water pressure p_w upon undrained shearing, especially when approaching to the critical state line. We recommend to calibrate this parameter by trial and error given some undrained tests.

The parameter R corresponds to the amplitude of the threshold strain which encloses the elastic locus of the material. It can be determined from a secant shear modulus degradation curve. When this test is not available, a value $R = 10^{-4}$ is recommended to describe the elastic behavior of clays. This value has proved to provide numerical stability in finite element implementations [16]. The parameter β_h controls the strain amplitude required to reach the mobilized states. A relation for β was provided in [16] and reads:

$$\beta = \frac{\sqrt{6}\,R\,(\log(4) - 2\log(1 - r_h))}{6\,\Delta\varepsilon_s - \sqrt{6}\,R\,(3 + r_h)} \tag{38}$$

where $\Delta\varepsilon_s$ is the deviatoric strain amplitude and $r_h \approx 0.99$ is a factor which defines how close tensor $\mathbf{c}$ is to its bounding condition $r_h = \|\mathbf{c}\|/\|\mathbf{c}_b\|$. The parameters χ_0 and $\chi_{\max}$ control the degradation curve shape of the secant shear modulus G_{sec}. According to Poblete et al. [43], parameter χ_0 should be calibrated on a single or a few cycles ($N < 3$). Details of the determination of χ_0 were given in [19]. When the number of consecutive cycles under cyclic undrained triaxial test increases, the usage of curves showing the water pore pressure p_w against the number of cycles N is recommended in order to determine parameters $\chi_{\max}$ and C_a. Figure 14 shows the influence of these parameters in a curve fitting the Kaolin. While parameter $\chi_{\max}$ governs the accumulation rate for a large number of consecutive cycles, C_a controls how fast the accumulation is produced during the first cycles. A trial-and-error procedure is herein recommended to calibrate simultaneously these two parameters.

References

1. Anderson D, Richart F (1976) Effects of straining on shear modulus of clays. ASCE J Geotech Eng Div 102(9):975–987
2. Argyris J, Faust G, Szimmat J, Warnke P, William K (1974) Recent developments in finite element analyses of prestressed concrete reactor vessels. Nucl Eng Des 28:42–75
3. Atkinson J, Richardson D, Stallebrass S (1990) Effect of recent stress history on the stiffness of overconsolidated soil. Géotechnique 40(4):531–540
4. Atkinson, J, Sallfors, G (1991) Experimental determination of stress-strain-time characteristics in laboratory and in situ tests. General report to session 1. In: BGS (ed) 10th European conference on soil mechanics and foundation engineering, vol 3. Florence, pp 915–956
5. Avgerinos V, Potts D, Standing J (2016) The use of kinematic hardening models for predicting tunnelling-induced ground movements in London clay. Géotechnique 66(2):106–120
6. Bjerrum L (1967) Engineering geology of Norwegian normally-consolidated marine clays as related to settlements of buildings. Géotechnique 17:83–118
7. Borja R (1992) Generalized creep and stress relaxation model for clays. J Geotech Eng Div ASCE 118(11):1765–1786
8. Borja R, Kavazanjian E (1985) A constitutive model for the stress–strain-time behaviour of wet clays. Géotechnique 35(3):283–298
9. Burland J, Simpson B, St John H (1979) Movements around excavations in London Clay, design parameters in geotechnical engineering. In: BGS (ed) VII ECSMFE, vol 1. London, UK, pp13–29
10. Chatterjee S, White D, Randolph M (2012) Numerical simulations of pipe-soil interaction during large lateral movements on clay. Géotechnique 62(8):693–705
11. Chen J (2017) A monotonic bounding surface critical state model for clays. Acta Geotech 12(1):225–230
12. Clayton C (2011) Stiffness at small strain: research and practice. Géotechnique 61(1):5–37
13. Dafalias Y (1986) Bounding surface plasticity. I: mathematical foundation and hypoplasticity. J Eng Mech ASCE 112(9):966–987
14. Ellison K, Soga K, Simpson K (2012) A strain space soil model with evolving stiffness anisotropy. Géotechnique 62:627–641
15. Fellin W (2013) Extension to Barodesy to model void ratio and stress dependency of the K_0 value. Acta Geotech 8(5):561–565
16. Fuentes (2014) W Contributions in Mechanical Modelling of Fill Materials. PhD thesis, Institut für Bodenmechanik und Felsmechanik, Karlsruher Institut für Technologie, Karlsruhe, Heft 179
17. Fuentes W, Hadzibeti M, Triantafyllidis T (2016) Constitutive model for clays under the ISA framework. In: Triantafyllidis T (ed) Holistic simulation of geotechnical installation processes. Lecture notes in applied and computational mechanics, vol 80. Springer International Publishing, Switzerland, pp 115–129
18. Fuentes W, Triantafyllidis T (2013) Hydro-mechanical hypoplastic models for unsaturated soils under isotropic stress conditions. Comput Geotech 51:72–82
19. Fuentes W, Triantafyllidis T (2015) ISA model: a constitutive model for soils with yield surface in the intergranular strain space. Int J Numer Anal Methods Geomech 39(11):1235–1254
20. Fuentes W, Triantafyllidis T, Lizcano A (2012) Hypoplastic model for sands with loading surface. Acta Geotech 7(3):177–192
21. Gudehus G (1979) A comparison of some constitutive laws for soils under radially symmetric loading and unloading. In: Wittke W (ed) 3rd International conference on numerical methods in geomechanics. Aachen, Germany, pp 1309–1323
22. Hadzibeti M (2016) Formulation and calibration of a viscous ISA model for clays. Master thesis, Karlsruhe Institute of Technology KIT. Institute of Soil Mechanics and Rock Mechanics IBF
23. Hardin B, Richart E (1963) Elastic wave velocities in granular soils. J Soil Mech Found Div ASCE 89(SM1):33–65
24. Herle I, Kolymbas D (2004) Hypoplasticity for soils with low friction angles. Comput Geotech 31(5):365–373
25. Hong P, Pereira J, Tang A, Cui Y (2016) A two-surface plasticity model for stiff clay. Acta Geotech 11:871–885
26. Huang W, Wu W, Sun D, Sloan S (2006) A simple hypoplastic model for normally consolidated clay. Acta Geotech 1(1):15–27
27. Jiang J, Ling H, Kaliakin V, Zeng X, Hung C (2016) Evaluation of an anisotropic elastoplastic viscoplastic bounding surface model for clays. Acta Geotech. doi:10.1007/s11440-016-0471-7
28. Karstunen M, Yin Z (2010) Modelling time-dependent behavior of murro test embankment. Géotechnique 60(10):735–749
29. Kolymbas D (1991) An outline of hypoplasticity. Arch Appl Mech 61(3):143–151
30. Kutter B, Sathialingam N (1992) Elastic-viscoplastic modelling of rate-dependent behaviour of clays. Géotechnique 42(3):427–441
31. Leinenkugel H Deformations- und Festigkeitsverhalten bindiger Erdstoffe. Experimentelle Ergebnisse und ihre physikalische Deutung. PhD thesis, Institut für Bodenmechanik und Felsmechanik, Universität Karlsruhe, Karlsruhe, 1978. Heft 66
32. Manzari M, Akaishi M, Dafalias Y (2002) A simple anisotropic clay plasticity model. Mech Res Commun 29(4):241–245
33. Manzari M, Papadimitriou A, Dafalias Y (2006) Saniclay: simple anisotropic clay plasticity model. Int J Numer Anal Methods Geomech 30(4):1231–1257
34. Masin D (2005) A hypoplastic constitutive model for clays. Int J Numer Anal Methods Geomech 29(4):311–336
35. Masin D (2006) Hypoplastic models for fine-grained solid. PhD thesis, Charles University, Prague
36. Medicus G, Fellin W (2016) An improved version of Barodesy for clay. Acta Geotech. doi:10.1007/s11440-016-0458-4
37. Niemunis A (2003) Habilitation, monografia 34. Ruhr-University Bochum
38. Niemunis A, Grandas-Tavera CE, Prada-Sarmiento LF (2009) Anisotropic visco-hypoplasticity. Acta Geotech 4(4):293–314
39. Niemunis A, Herle I (1997) Hypoplastic model for cohesionless soils with elastic strain range. Mech Cohes Frict Mater 2(4):279–299

40. Niemunis A, Krieg S (1996) Viscous behaviour of soil under oedometric conditions. Can Geotechn J 33(1):159–168
41. Norton F (1929) The creep of steel at high temperatures. Mc Graw Hill Book Company, New York
42. Oka F, Leroueil S, Tavenas F (1989) A constitutive model for natural soft clay with strain softening. Soils Found 29:54–66
43. Poblete M, Fuentes W, Triantafyllidis T (2016) On the simulation of multidimensional cyclic loading with intergranular strain. Acta Geotech 11(6):1263–1285
44. Raude S, Laigle F, Giot R, Fernandes R (2016) A unified thermoplastic/viscoplastic constitutive model for geomaterials. Acta Geotech 11:849–869
45. Schofield A, Wroth P (1968) Critical state soil mechanics. Mc Graw Hill, London
46. Seidalinov G, Taiebat M (2014) Bounding surface saniclay plasticity model for cyclic clay behavior. Int J Numer Anal Methods Geomech 38(7):702–724
47. Shibuya S, Hwang S, Mitachi T (1997) No access elastic shear modulus of soft clays from shear wave velocity measurement. Géotechnique 47(3):593–601
48. Simo J, Hughes T (1998) Computational inelasticity. Springer, New York
49. Simpson B (1992) Retaining structures: displacement and design. Géotechnique 42(4):541–576
50. Stolle D, Bonnier P, Vermeer P (1999) A soft soil model and experiences with two integration schemes. In: 6th International symposium on numerical models in geomechanics (NUMOG VI). A.A. Balkema, Amsterdam, the Netherlands, pp 123–128
51. Taiebat M, Dafalias Y, Peek R (2010) A destructuration theory and its application to saniclay model. Int J Numer Anal Methods Geomech 34(10):1009–1040
52. Tsai C, Mejia L, Meymand P (2014) A strain-based procedure to estimate strength softening in saturated clays during earthquakes. Soil Dyn Earthq Eng 66:191–198
53. Vermeer P, Neher H (1999) A soft soil model that accounts for creep. In: The plaxis symposium on beyond 2000 in computational geotechnics. Amsterdam, the Netherlands, pp 249–262
54. Vlahos G, Cassidy M, Martin M (2011) Numerical simulation of pushover tests on a model jack-up platform on clay. Géotechnique 61(11):947–960
55. Weifner T, Kolymbas D (2007) A hypoplastic model for clay and sand. Acta Geotech 2(2):103–112
56. Whittle A, Kiavvadas M (1994) Formulation of MIT-E3 constitutive model for overconsolidated clays. J Geotech Eng Div ASCE 120(1):173–198
57. Wichtmann T (2016) Soil behaviour under cyclic loading—experimental observations, constitutive description and applications. Habilitation, Karlsruhe Institute for Technology KIT, Institute of Soil Mechanics and Rock Mechanics IBF. Heft No. 81
58. Wichtmann T (2015) Explicit accumulation model for non-cohesive soils under cyclic loading. Dissertation, Schriftenreihe des Institutes für Grundbau und Bodenmechanik der Ruhr-Universität Bochum, Heft 38. www.rz.uni-karlsruhe.de/~gn97/, 2005
59. Wolffersdorff P (1996) A hypoplastic relation for granular materials with a predefined limit state surface. Mech Cohes Frict Mater 1(3):251–271
60. Wu W, Bauer E (1994) A simple hypoplastic constitutive model for sand. Int J Numer Anal Methods Geomech 18(12):833–862
61. Yin J, Graham J (1994) Equivalent times one-dimensional viscoplastic modelling of time-dependent stress-strain behaviour of clays. Can Geotech J 31(1):42–52
62. Yin J, Graham J (1999) Elastic viscoplastic modelling of the time-dependent stress-strain behaviour of soils. Can Geotech J 36(4):736–745
63. Yin Z, Jin Y, Shen S, Huang H (2016) An efficient optimization method for identifying parameters of soft structured clay by an enhanced genetic algorithm and elastic-viscoplastic model. Acta Geotech. doi:10.1007/s11440-016-0486-0